Combined Analysis of NASA's High Efficiency Megawatt Motor and Its Converter

Matthew Granger[1], Aaron Anderson[2], John M. Maroli[3], Thomas Tallerico[4], and Justin J. Scheidler [5]
NASA Glenn Research Center, Cleveland, OH, 44135, USA

NASA's High Efficiency Megawatt Motor (HEMM) is being developed to achieve the performance needed by single aisle class electrified aircraft. It is a 1.4 MW electric machine designed as a generator for NASA's STARC-ABL concept vehicle. It has performance objectives of greater than 16 kW/kg electromagnetic specific power and efficiency of greater than 98%. The key enabling technology for HEMM's high performance metrics is a superconducting rotor cooled by an integrated cryocooler. HEMM's integrated cryocooler is being designed to only lift 50 W of heat at its target 50 K cold tip operating temperature. HEMM's superconducting rotor therefore needs to have essentially zero electromagnetic losses in order to stay below the 50 W heat rejection limit of the cryocooler. This paper presents the combined analysis of HEMM and a preliminarily designed HEMM converter to analyze the rotor loss impact of several potential converter filter topologies. The analysis results point to interleaving and series inductance filters not being sufficient to suppress switching harmonic caused rotor loss. Paths forward to develop a converter to eliminate rotor loss are discussed.

I. Nomenclature

A	=	area	t	=	time
B	=	magnetic flux density	T	=	time period of magnetic flux repetition
d	=	wire diameter	w	=	tangential width of a component
I_n	=	current through coil n	V	=	volume
l	=	axial length of component	V_n	=	voltage on winding n
L	=	overall length	α	=	Steinmetz frequency coefficient
L_{mn}	=	coupling inductance between coils m and n	β	=	Steinmetz flux density coefficient
			γ	=	Steinmetz coefficient
L	=	inductance matrix	γ_1	=	modified Steinmetz coefficient
M	=	mass	θ	=	rotor angle
P	=	power loss	ρ	=	resistivity
R_n	=	resistance of coil n			

II. Introduction

Advances in megawatt class electric motor power density and efficiency are required to enable electric aircraft for single aisle class civil transportation vehicles. NASA's High Efficiency Megawatt Motor (HEMM) is a 1.4 MW

[1] Electrical Power Systems Engineer, Power Management and Distribution Branch, matthew.granger@nasa.gov.
[2] Electrical Systems Engineer, Diagnostics and Electromagnetics Branch, aaron.d.anderson-1@nasa.gov.
[3] Software Systems Engineer, Flight Software Branch, john.m.maroli@nasa.gov.
[4] Research Engineer, Rotating and Drive Systems Branch, thomas.tallerico@nasa.gov.
[5] Research Mechanical Engineer, Rotating and Drive Systems Branch, justin.j.scheidler@nasa.gov.

slotless partially superconducting machine being developed at NASA Glenn Research Center to meet the performance requirements of single aisle class passenger transport electric aircraft. The current version of HEMM is designed to meet the requirements of the two generators on NASA's STARC-ABL concept aircraft [1] [2]. Specifically, the targets are electromagnetic specific power greater than 16 kW/kg and efficiency greater than 98%. The benefits of HEMM in an integrated system are presented in [3].

The development of HEMM has been discussed in a number of publications to date [1] [2] [3] [4] [5] [6] [7] [8] [9] [10] [11] [12] [13]. The key enabling technology for HEMM's high performance metrics is a wound field superconducting rotor that is cooled by a cryocooler integrated into HEMM's shaft. HEMM's cryocooler is only designed to lift 50 watts of heat at its 50 K nominal cold tip operating temperature. Therefore, for HEMM to work properly and achieve its targeted performance metrics, the rotor must have essentially zero electromagnetic losses. At the machine level with perfectly sinusoidal current waveforms, this low loss level is achieved through the use of a slotless 9 phase stator. The development of the slotless stator design and analysis of the rotor losses with perfect sinusoidal current waveforms was presented in [11].

In this paper, preliminary analysis of HEMM supplied by real converter waveforms is presented. The results of this analysis points toward needed technology advancement to close the combined HEMM and HEMM converter system. Section III of this paper discusses the preliminary HEMM converter design. Section IV presents the power electronics simulation and resulting waveforms. Section V presents rotor loss analysis methodology. Section VI discusses the results of the analysis and the forward path to close the HEMM system design.

III. HEMM Converter Preliminary Concept Design

The design goal of the HEMM converter is to make component and topology choices which enable the achievement of three key performance parameters: high efficiency (99.5%), high power density (20 kW/kg), and low harmonic distortion to limit HEMM rotor loss. These three parameters are typically in conflict with one another when trading converter designs, and therefore topology decisions must carefully achieve balance between them. The preliminary design of the HEMM converter is a scaled up version of the 250 kW converter presented in [14]. In that converter design, low harmonic distortion and high performance are achieved through two key topology choices: multilevel switching and interleaving filters.

The multilevel switching architecture both lowers the current waveform distortion and enables the use of high efficiency and readily available off-the-shelf Silicon Carbide MOSFETs in a higher voltage system than the switches are rated to. The very low switching losses and low conduction losses of the Silicon Carbide MOSFETs enables the high efficiency target.

The interleaving filters enable equal current sharing among parallel FETs and provides significant current waveform distortion reduction. These filters are designed with high inductance to minimize circulating current in the converter and the associated losses. Correspondingly substantial weight allocation is afforded to the interleave output filters. Custom magnetic material developed by the NASA Glenn advanced magnetic materials group is used to minimize the mass and loss impact of these filters.

Another vital aspect of the converter's design is its controller. For instance, the HEMM is very susceptible to spatial harmonics due to the machine's low inductance. Because of this, small perturbations in the machine's back-emf can lead to large amplitude current harmonics. In particular the 3^{rd}, 5^{th}, and 7^{th} harmonics need to be suppressed in order to avoid the associated rotor loss. A harmonic controller is incorporated to accomplish this harmonic suppression, which augments the classic vector control.

The following section discuss the development of a model of the HEMM converter preliminary controller design.

IV. Converter-Motor Model (Simulink)

A. Converter Model

A transient electrical simulation is required to generate a stator current waveform of sufficient fidelity to be used in rotor loss calculations. A Simulink implementation of the integrated converter, controller, and motor system is shown in Fig. 1. The converter model generates a 9-phase voltage signal with any selected number of interleaves and switch levels. The HEMM motor model incorporates the FEA generated back-emf harmonics and inductance matrix from Appendix A. The output of the simulation is the stator current waveform, which contains the spatial and temporal harmonics relevant to the rotor loss study.

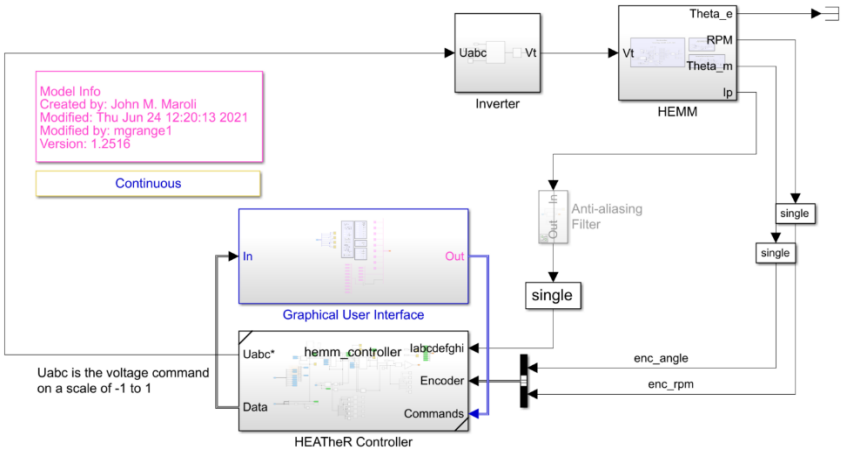

Fig. 1 Top-level block diagram of the HEMM Simulink simulation.

To implement the harmonic controller, the 9 phase Park and Clark transformations were adapted to generate d and q axis current components in these harmonic reference frames, in addition to the typical d and q components at the fundamental rotor reference frame. An example of this adapted Park transform is shown in Eq. 1. These additional d and q components are regulated to zero using additional PI controllers.

$$f_{dq} = \begin{bmatrix} \sin(\varphi) & \cos(\varphi) & 0 & 0 & 0 & 0 & 0 & 0 & 0 \\ -\cos(\varphi) & \sin(\varphi) & 0 & 0 & 0 & 0 & 0 & 0 & 0 \\ 0 & 0 & \sin(3\varphi) & \cos(3\varphi) & 0 & 0 & 0 & 0 & 0 \\ 0 & 0 & -\cos(3\varphi) & \sin(3\varphi) & 0 & 0 & 0 & 0 & 0 \\ 0 & 0 & 0 & 0 & \sin(5\varphi) & \cos(5\varphi) & 0 & 0 & 0 \\ 0 & 0 & 0 & 0 & -\cos(5\varphi) & \sin(5\varphi) & 0 & 0 & 0 \\ 0 & 0 & 0 & 0 & 0 & 0 & \sin(7\varphi) & \cos(7\varphi) & 0 \\ 0 & 0 & 0 & 0 & 0 & 0 & -\cos(7\varphi) & \sin(7\varphi) & 0 \\ 0 & 0 & 0 & 0 & 0 & 0 & 0 & 0 & 1 \end{bmatrix} f_{abcdefghi} \quad (1)$$

The simulation is also simulates converter-generated temporal harmonics. The characteristics of this noise are determined by the topology of the converter, particularly the number of switching levels and interleave filters used. Both of these converter technologies help to decrease the amplitude of the temporal harmonics by decreasing the voltage step size and pushing the frequency content up to higher ranges. An example of a phase terminal voltage waveform produced by the simulated converter is shown in Fig. 2.

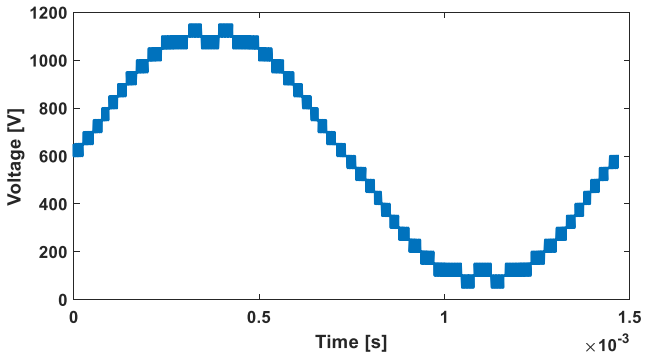

Fig. 2 Terminal voltage produced by HEMM converter (12 interleaves, 3 level).

B. Results

Simulation results showing stator current waveforms and the influence of the harmonic controller are shown in Fig. 3 and Fig. 4. Fig. 3 shows the elimination of the low-frequency content in the stator current, leaving only the remaining temporal harmonics. Fig. 4 shows the relevant d and q axis current plots in a transient simulation running the motor up to full speed, and the ability of the harmonic controller to regulate those components in steady state.

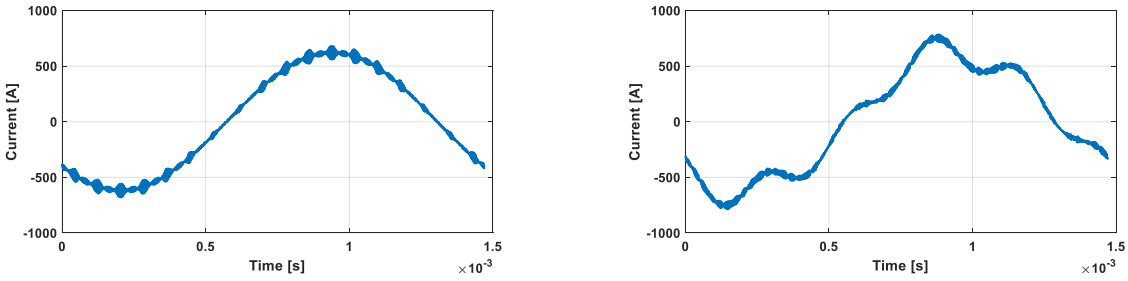

Fig. 3 Stator current (a) with and (b) without the harmonic controller.

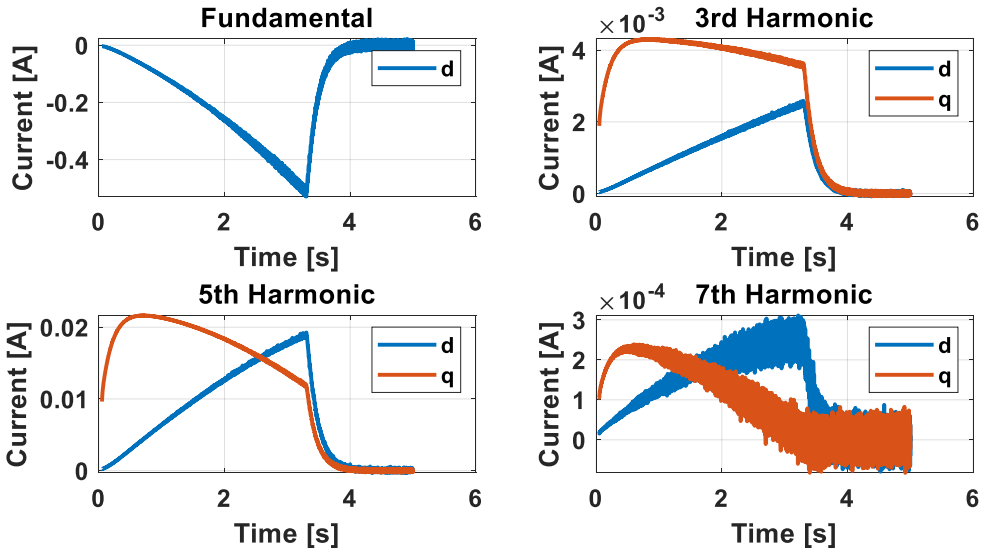

Fig. 4 Relevant Id and Iq currents converging due to harmonic controller. Initial error before t=3.5s due to speed ramping towards setpoint.

Fig. 5 shows the time and frequency domain representations of the stator current waveform. The action of the interleaving is apparent in the frequency domain in that the center of the fundamental temporal noise occurs at a frequency which is a multiple of the converter switching frequency, which allows the motor's inductance to more effectively filter the noise.

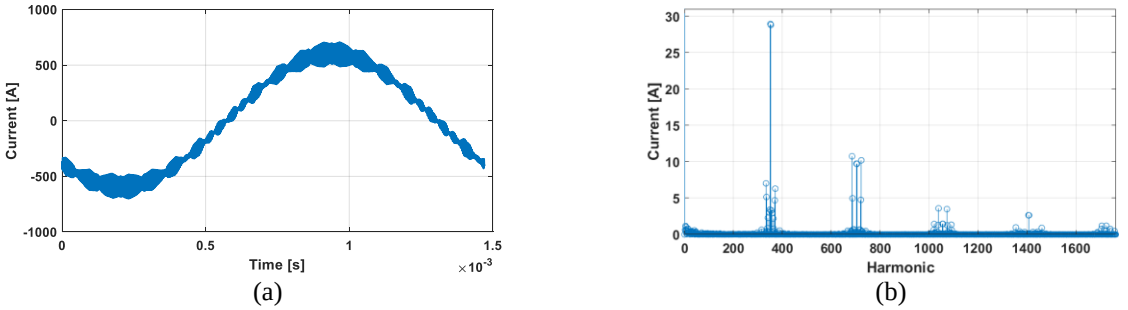

Fig. 5 Stator current with switching noise in (a) time and (b) frequency. Fundamental omitted in frequency domain. Switching frequency 59.84kHz, fundamental frequency 680Hz, 4 interleaves.

V. Rotor Loss Model

To evaluate rotor loss, transient electromagnetic finite element analysis of a 2D cross section of the motor spanning one rotor pole pair was used. Stator current wave forms were taken from the converter model. The rotor components were modeled as conductive bodies. All rotor bodies were modeled as completely electrically isolated from one another with a small artificial gap between components. The rotor coils were modeled as solid blocks of copper and the titanium rotor structural components were modeled as a single domain. Since the rotor coils fully saturate the rotor iron, the only rotor iron loss calculated were the eddy currents. Modeling the rotor components as fully isolated from one another is optimistic but made convergence of the model more reliable for the number of current waveforms run through the loss model.

The simulation was first solved statically to create an initial condition and then a short transient simulation was run to capture the effect of the stator harmonics on the rotor losses. The transient analysis was run for only 5E-5 s and results were output with a 1E-7 s resolution. A graphic showing the FEA model at a snapshot in time is shown in Fig. 6.

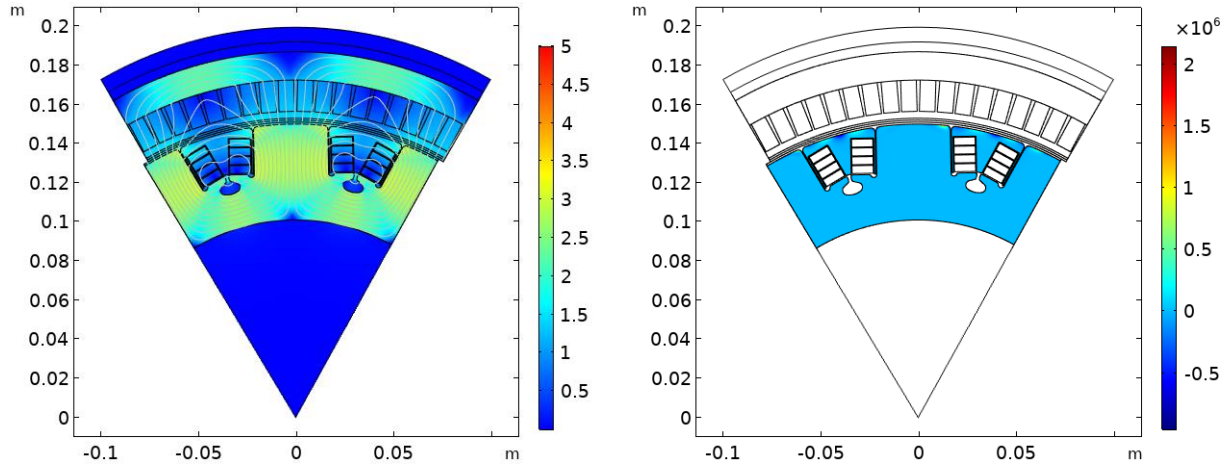

Fig. 6 FEA model. Example field distribution right and example eddy current response in the rotor components left.

In Fig. 6, rotor eddy currents are shown to be concentrated at the outer radial edge of the rotor titanium and iron components. This concentration at the edge corresponds to the skin depth of the high frequency stator current waveform harmonics. Losses in the rotor model were evaluated in rotor titanium and iron components at all time steps. Fig. 7 shows how the loss varies over the simulation time.

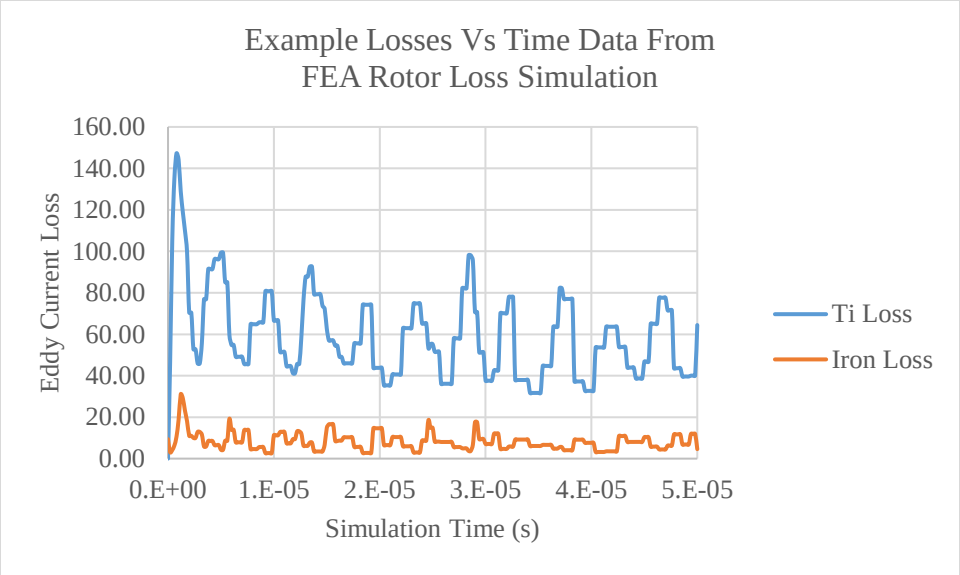

Fig. 7 Example loss profiles for the titanium and iron components over the simulation.

In Fig. 7 the losses are shown to start with a significant transient which decays with simulation time. This transient decay of the loss is a modeling artifact due to the static simulation used to create the initial condition for the transient simulation which has no eddy currents or electrical field in the rotor. Rotor loss values reported in Section VI are reported as the average of the last 25 time steps of the simulations. There is a great deal of uncertainty in the values reported as the simulation is attempting to calculate losses on the order of 10's of watts in a 1.4 megawatt machine. The results are however sufficient to show that there is rotor loss caused by the inverter harmonics and provide some relative performance information for various converter filter options.

VI. HEMM and Converter Results

Because of the effectiveness of the harmonic controller implemented in the preliminary HEMM converter design, only the temporal harmonics in the converter waveform are large enough to produce rotor eddy current loss. The preliminary concept design for the HEMM targeted low rotor loss through the minimization of total harmonic distortion (THD) created by these temporal harmonics in the converter current waveform. Initial rotor loss simulations found that THD and rotor loss did not always correlate. A more accurate analytical method of predicting the effectiveness of different filtering configurations on rotor loss was found to be a method based on the Steinmetz classical eddy current relationship:

$$P = kf^2B^2,$$

where P is the rotor loss, k is a constant depending on the shape and conductivity of the material, f is frequency, and B is the peak of the time varying magnetic flux density that penetrates the magnetic component.

The sum of the Stienmetz equation over all harmonics in a converter waveform was used to estimate the effect of various filtering techniques on rotor loss. The calculated effectiveness of different filtering techniques using this Stienmetz based approach are shown in Fig. 8. Because of the inaccuracy in the proportionality constant (k) used in this estimate only relative comparisons are made to establish trends. Fig. 8 (a)-(c) show that all the techniques implemented in the preliminary HEMM converter design to reduce THD (interleaving, multilevel, and series inductance) are effective, but suffer from diminishing returns in effectiveness. Fig. 8 (d) shows increasing switching frequency as a filtering technique to be ineffective due to the increased coupling at higher frequencies balancing out the decreased magnetic flux magnitude from increasing stator impedance.

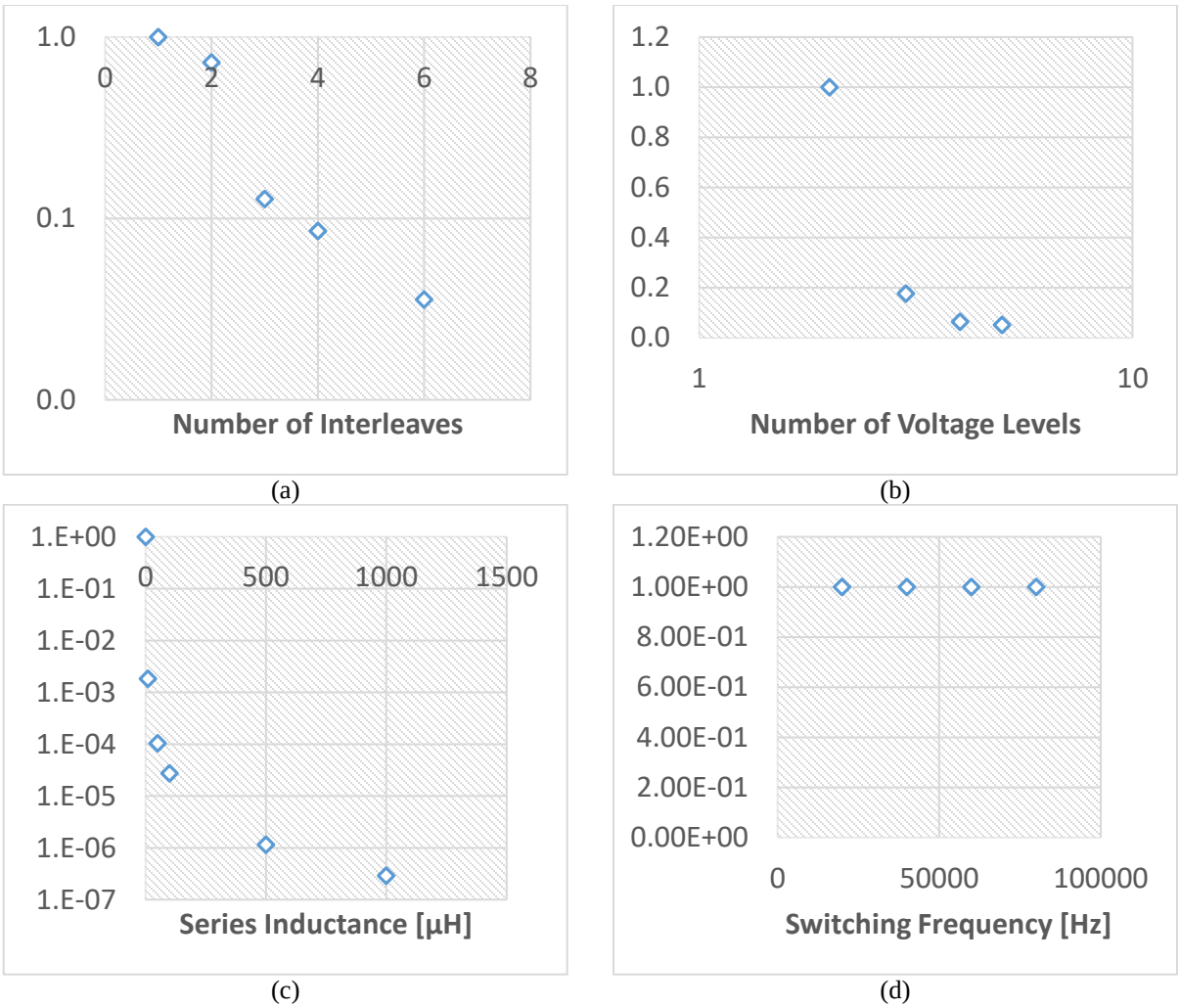

Fig. 8 Estimated rotor loss as a function of (a) number of interleaves, (b) number of voltage levels, (c) inductance in series with motor phases, and (d) switching frequency. Each plot normalized to left-most point.

These trends are confirmed by the FEA model calculated rotor loss for several different configurations of interleaving and additional series inductance, as shown in Fig. 9 and Fig. 10. The results confirm the trend of diminishing returns in the effectiveness of both interleaving and additional series inductance as techniques to reduce rotor loss. The results also point to none of these original techniques implemented in the HEMM converter concept design to reduce rotor loss being a viable path to close the design within the target mass of the HEMM converter.

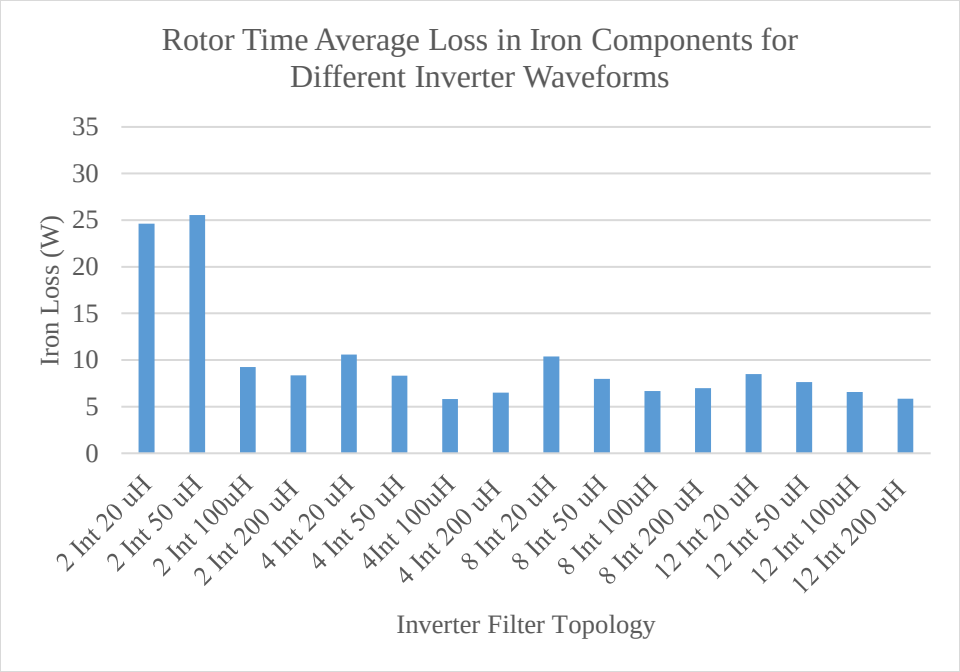

Fig. 9 FEA calculated losses in rotor iron from different converter filtering techniques.

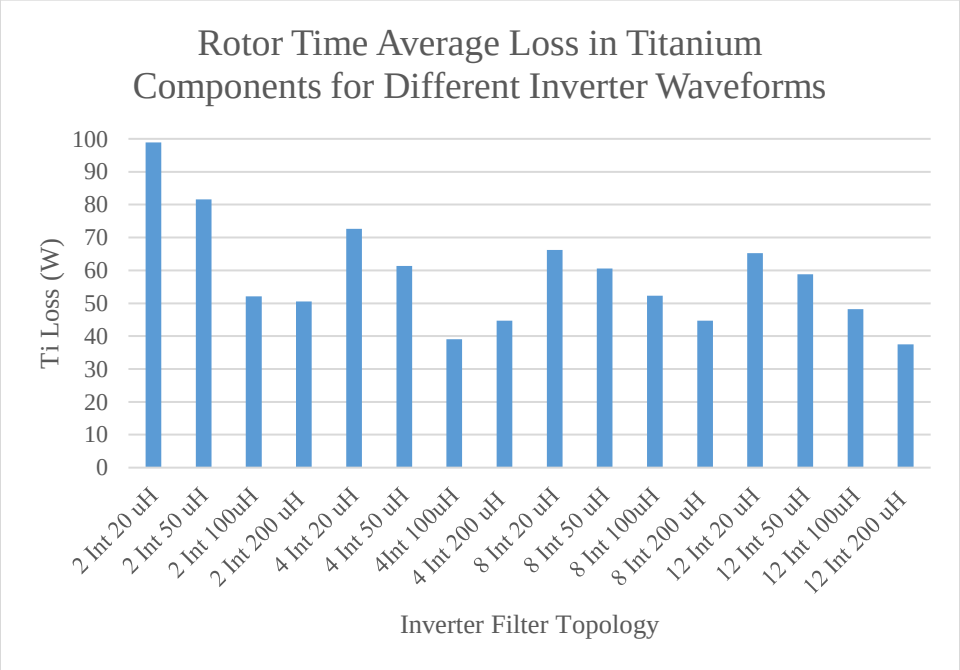

Fig. 10 FEA calculated losses in rotor titanium components from different converter filtering techniques.

These results indicate that a filtering technique focused on preventing the generation of high frequency current may not be practical. A technique to divert high frequency content away from the stator, such as a high frequency resonant converter combined with a lightweight LCL output filter, may be a practical solution for achieving sufficiently low rotor loss. This technique will be further investigated.

VII. Conclusion

In this paper, combined analysis of HEMM and the preliminary design of the HEMM converter was presented to assess the system's potential to achieve the low rotor loss requirement of the HEMM motor. The results show that the technologies implemented in the preliminary converter design do not sufficiently reduce inverter current waveform harmonics to meet the low rotor loss target. These initial technologies were selected with the goal of minimizing the THD of the inverter waveform. The analysis presented here however points to a metric based on a Stienmetz classical eddy current formulation being a better option for ranking different converter technologies impact on rotor loss. Going forward a resonant converter topology will be explored as a possible path to close the HEMM system within the high performance targets of the system. Future work will also target evaluating whether using a rotor eddy current shield in partially superconducting machines leads to a more optimum overall system.

VIII. Appendix

A. Motor Equivalent Circuit Model

In order to enable combined analysis of the HEMM motor and converter, an equivalent circuit model of the HEMM motor had to be developed. Due to HEMM being a 9 phase machine the development of this equivalent circuit model is not straight forward. The following sections discuss how the model was developed and key parameters were estimated.

1. Modeling approach

At a fixed position, the motor is effectively a multi-port transformer with saturated iron. Voltage, current, resistance, and inductance are described by matrix equation

$$\begin{bmatrix} V_1 \\ V_2 \\ \vdots \\ V_9 \end{bmatrix} = \begin{bmatrix} R_1 & 0 & \cdots & 0 \\ 0 & R_2 & \cdots & 0 \\ \vdots & \vdots & \ddots & \vdots \\ 0 & 0 & \cdots & R_9 \end{bmatrix} \cdot \begin{bmatrix} I_1 \\ I_2 \\ \vdots \\ I_9 \end{bmatrix} + \begin{bmatrix} L_{11} & L_{12} & \cdots & L_{19} \\ L_{21} & L_{22} & \cdots & L_{29} \\ \vdots & \vdots & \ddots & \vdots \\ L_{91} & L_{92} & \cdots & L_{99} \end{bmatrix} \cdot \frac{d}{dt} \begin{bmatrix} I_1 \\ I_2 \\ \vdots \\ I_9 \end{bmatrix} \tag{2}$$

The resistances in Eq. 2 can easily be calculated through analytical equations, but to calculate the inductances currents have to be carefully applied in an FEA simulation of the machine. The 2D FEA model of HEMM used to complete this calculation is shown in Fig. 11. The symmetry of the 12 pole machine is used to reduce model size by only model one sixth of the machine cross section. Additionally, each slot is modeled as a single turn for simplicity even though current planned construction of the HEMM stator consists of 2 turns per slot.

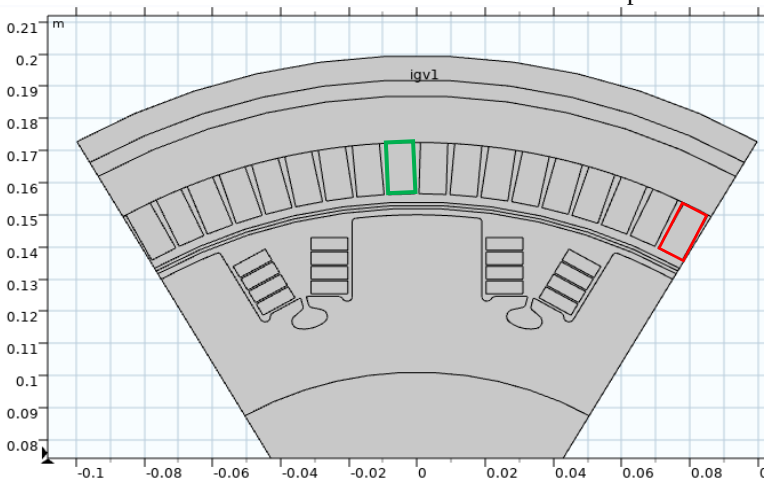

Fig. 11 2d FEA screenshot. As shown, the rotor angle is defined as zero. The stator windings with green and red boxes are defined as phase one with positive current into and out of the page, respectively.

The first step in calculating the inductance is to calculate the resistance of the windings in the FEA simulation so the resistive portion of the voltage can be removed from the voltage results in subsequent simulations. To do this full

current is applied to the first stator coil and zero current to all other coils in a stationary FEA simulation. In this simulation, the time derivative of current is zero so the first row of Eq. 2 can be extracted through the equation

$$R_1 = \frac{V_1}{I_1}. \tag{3}$$

The resistance calculated with this approach only includes the active portion of the motor. The end-windings and the effect of the litz wire twist and fill percentage is not captured. Correspondingly this resistance value is only useful for calculating the inductance of the machine from FEA.

To complete extraction of the inductance values, a current ramp is applied to one stator winding and zero current is applied to all other windings in a transient simulation. By observing the induced voltages on each winding, the values of the first row of the inductance matrix in Eq. 2 are calculated using the following equations:

$$V_1 = R_1 I_1 + L_{11}\frac{dI_1}{dt}$$
$$L_{11} = (V_1 - R_1 I_1)/\frac{dI_1}{dt} \tag{4}$$

$$V_n = L_{n1}\frac{dI_1}{dt}$$
$$L_{n1} = \frac{V_n}{\frac{dI_1}{dt}}, \mathrm{n} = 2,3,\ldots,9. \tag{5}$$

This current ramp simulation is repeated at various rotor angles to determine the inductance variation as a function of rotor saliency. The following section presents the results of these simulations.

2. Inductance Calculation Results

Fig. 12 the inductances calculated using Eqs. 4-5 with a transient current applied to coil 1 at a set rotor position. After a startup transient, the inductances settle to consistent values, as expected. The results of simulations at other rotor positions showed similar settling times. Negative inductance values shown in Fig. 12 indicate that the winding direction in the actual motor is opposite of how it is modeled in the FEA simulation. As expected, the self-inductance L_{11} is larger than any of the coupling inductances and the coupling inductance between each pair of coils is related to the physical distance between the coils. The values from these current transient simulations corresponding to only one winding phase are enough to populate the inductance matrix for the machine as each subsequent phase has the same inductances just offset based on the relative position of the other phases to it in the machine.

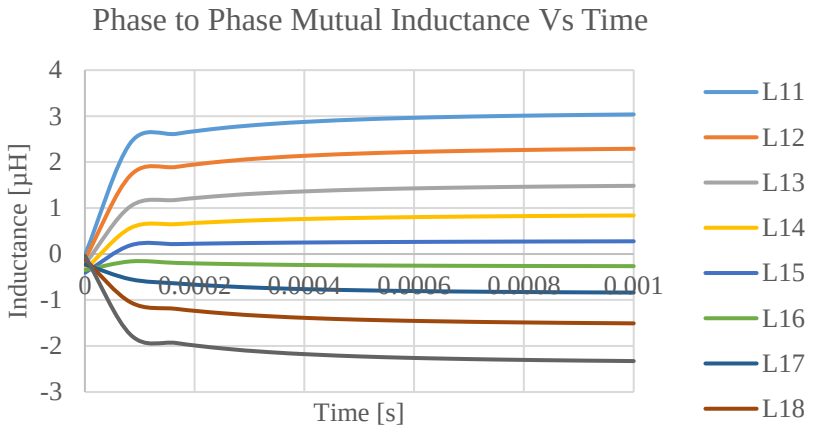

Fig. 12 Simulated inductances over time in transient simulation for $\boldsymbol{\theta = 0}$.

Because of the rotor's salient poles, there is variation in inductance matrix as a function of rotor angular position. However, because the superconducting coils of the rotor fully saturate the rotor poles during machine operations, the variation in inductance with rotor position is small. Fig. 13 shows the inductances as a function of rotor angle. The time average values used to populate the inductance matrix are given in Table 1.

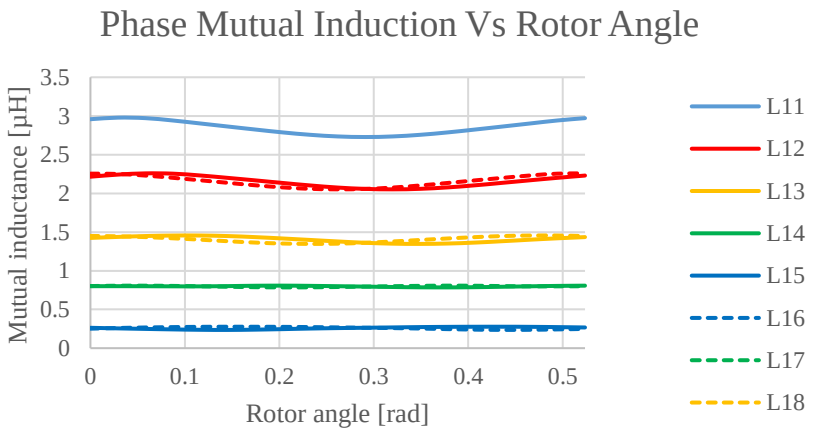

Fig. 13 Inductances as a function of rotor angle (θ).

Table 1 Time average inductances

Coil pair	Position average inductance [µH]
11	2.85
12	2.16
13	1.41
14	0.80
15	0.26
16	0.26
17	0.80
18	1.41
19	2.16

3. Machine Back EMF

With the resistance and inductance matrix define, the FEA model was then used to predict the back-EMF generated on each coil at HEMM's nominal operating speed of 6800 RPM. Fig. 14 shows the back EMF from this transient simulation.

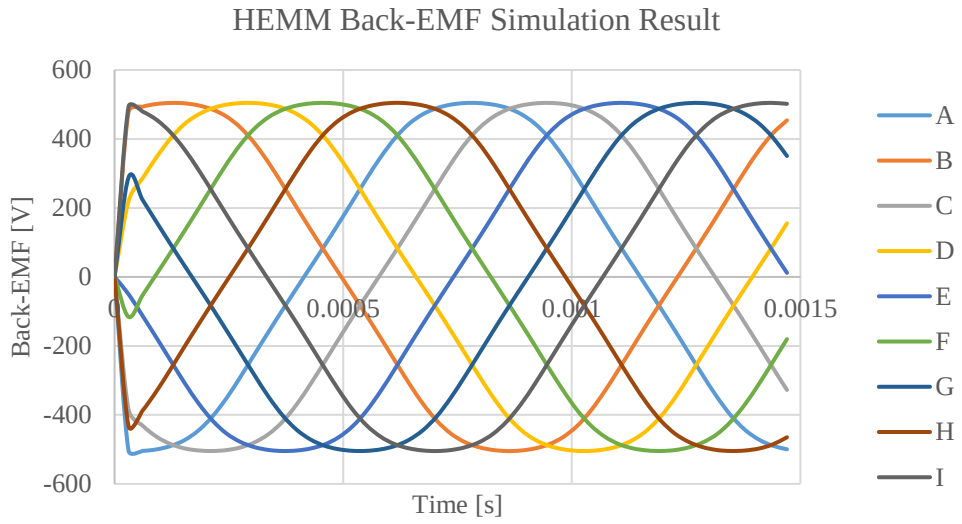

Fig. 14 Phase-to-neutral back-EMF generated by each coil.

Acknowledgments

This work was supported by Power and Propulsion Subproject within the Advanced Air Transport Technology Project of NASA's Aeronautics Research Mission Directorate. Additional support was provided by the Convergent Aeronautics Solutions Project of NASA's Aeronautics Research Mission Directorate. The authors would like to thank Pete Kascak for his technical guidance, as well as for laying the foundation of much of this work.

References

[1] R. H. Jansen, Y. De Jesus-Arce, P. Kascak, R. Dyson, A. Woodworth, J. J. Sheidler, R. Edwards, E. Stalcup, J. Whilhite, K. Duffy, P. Passe and S. McCormick, "High Efficiency Megawatt Motor Conceptual Design," in *AIAA Propulsion and Energy Forum*, Cincinnati, 2018.

[2] R. H. Jansen, P. Kascak, R. Dyson, A. Woodworth, J. Scheidler, A. D. Smith, T. Tallerico, Y. De Jesus-Arce, D. Avanesian, K. Duffy, P. Passe and G. Szpak, "High Efficiency Megawatt Motor Preliminary Design," in *AIAA/IEEE Electric Aircraft Technologies Synmposium*, Indianapolis, 2019.

[3] S. L. Schnulo, J. W. Chapman, P. Hanlon, H. Hasseeb, R. Jansen, D. Sadey, E. Sozer, J. Jensen, D. Maldonado, K. Bhamidapati, N. Heersema, K. Antcliff, Z. J. Frederick and J. Kirk, "Assessment of the Impact of an Advanced Power System on a Turboelectric Single-Aisle Concept Aircraft," in *AIAA Propulsion and Energy 2020 Forum*, Virtual, 2020.

[4] K. P. Duffy, P. J. Passe, R. W. Dyson and R. H. Jansen, "Design Analysis and Testing of the HEMM Cryocooler Linear Motor," in *AIAA/IEEE Electrified Aircraft Technologies Symposium*, New Orleans, 2020.

[5] R. W. Dyson, R. H. Jansen, K. P. Duffy and P. J. Passe, "High Efficiency Megawatt Machine Rotating Cryocooler Conceptual Design," in *AIAA Propulsion and Energy Forum*, Indianapolis, 2019.

[6] R. Jansen, J. J. Sheidler, T. Tallerico, P. Kascak, A. Woodworth, A. Smith, R. Dyson, W. Sixel, J. T. Thompson, E. Stalcup, Y. De Jesus-Arce, D. Avanesian, K. Duffy, P. Passe and G. Szpak, "High Efficiency Megawatt Motor Risk Reduction Activities," in *AIAA/IEEE Electric Aircraft Technologies Sumposium*, Virtual, 2020.

[7] G. Sapak, A. Smith, J. T. Thompson, A. Woodworth and R. Jansen, "High Efficiency Megawatt Motor Thermal Stator Preliminary Design," in *AIAA/IEEE Electrified Aircraft Technologies Symposium*, New Orleans, 2020.

[8] J. J. Scheidler, "Preliminary Design of the Superconducting Rotor for NASA's High-Efficiency Megawatt Motor," in *AIAA Propulsion and Energy Forum*, Cincinnati, 2018.

[9] J. J. Scheidler and T. F. Tallerico, "Design, Fabrication, and Critical Current Testing of No-Insulation Superconducting Rotor Coils for NASA's 1.4 MW High-Efficiency Megawatt Motor," in *AIAA/IEEE Electric Aircraft Technologies Symposium*, Cincinnati, 2018.

[10] J. J. Sheidler, T. F. Tallerico, W. A. Miller and W. Torres, "Progress Toward the Critical Design of the Superconducting Rotor for NASA's 1.3 MW High-Efficiency Electric Machine," in *AIAA/IEEE Electric Aircraft Technologies Symposium*, Indianapolis, 2019.

[11] T. Tallerico, J. J. Sheidler, D. Lee and K. S. Haran, "Electromagnetic Redesign of NASA's High Efficiency Megawatt Motor," in *AIAA/IEEE Electric Aircraft Technologies Symposium*, Virtual, 2020.

[12] A. Woodworth, A. Smith, R. Jansen and G. Szpak, "Select Variables Affecting Thermal System Design of a Liquid Cooled Stator," in *AIAA/IEEE Electric Aircraft Technologies Symposium* , Virtual, 2020.

[13] A. A. Woodworth, A. Smith, W. Sixel, R. Edwards, R. Jansen, S. McCormick, M. Robbie, G. Szpak, P. Naghipour and E.-S. Shin, "Thermal Analysis of Potted Litz Wire for High-Power-Density Aerospace Electric Machines," in *AIAA Propulsion and Energy Forum*, Indianapolis, 2019.

[14] M. Granger, D. Avanesian, R. Jansen, S. Kowalewski, A. Leary, R. Bowman, A. Dimston, E. Stalcup and W. Miller, "Design of a High Power Density, High Efficiency, Low THD 250kW Converter for Electric Aircraft," in *EATS*, 2021.

[15] R. H. Jansen, G. V. Brown, J. L. Felder and K. P. Duffy, "Turboelectric Aircraft Drive Key Performance Parameters and Functional Requirments," in *AIAA Propusion and Energy Forum*, Orlando, 2015.

[16] S. Rouho, T. Santa-Norkki, J. Kolehmainen and A. Arkkio, "Modeling Magnet Length in 2-D Finite Element Analysis of Electric Machnines," *IEE Transactions on Magnetics*, vol. 45, no. 8, 2009.

[17] M. T. Kakhki, J. Cros and P. Viarouge, "New Approach for Accurate Prediction of Eddy Current Losses in Laminated Material in the Presence of Skin Effect with 2-D FEA," *IEEE Transactions on Magnetics*, vol. 52, no. 3, 2016.

[18] J. R. Welstead and J. L. Flder, "Conceptual Design of a Single-Aisle Tuboelectric Commercial Transport with Fuselage Boundary Layer Ingestion," in *AIAA SciTech 2016*, San Diego, 2016.

[19] V. Venkatachalam, C. Sullivan, T. Abdallah and H. Tacca, "Accurate Predicition of Ferrite Core Loss with Non-Sinusoidal Waveforms Using only Steinmetz Parameters," in *Computers in Power Electronics*, Mayaguez, 2002.